



Combining Weather Station Data and Short-Term LiDAR Deployment to Estimate Wind Energy Potential with Machine Learning: A Case Study from the Swiss Alps

Fanny Kristianti¹ · Jérôme Dujardin^{1,2} · Franziska Gerber^{1,2} · Hendrik Huwald^{1,2} · Sebastian W. Hoch³ · Michael Lehning^{1,2}

Received: 24 December 2022 / Accepted: 21 March 2023 / Published online: 11 May 2023
© The Author(s) 2023

Abstract

Wind energy potential in complex terrain is still poorly understood and difficult to quantify. With Switzerland's current efforts to shift to renewable energy resources, it is now becoming even more crucial to investigate the hidden potential of wind energy. However, the country's topography makes the assessment very challenging. We present two measurement campaigns at Lukmanier and Les Diablerets, as representative areas of the complex terrain of the Swiss Alps. A general understanding of local wind flow characteristics is achieved by comparing wind speed measurements from a near-surface ultra-sonic anemometer and from light detection and ranging (LiDAR) measurements further aloft. The measurements show how the terrain modifies synoptic wind for example through katabatic flows and effects of local topography. We use an artificial neural network (ANN) to combine the data from the measurement campaign with wind speed measured by weather stations in the surrounding area of the study sites. The ANN approach is validated against a set of LiDAR measurements which were not used for model calibration and also against wind speed measurements from a 25-meter mast, previously installed at Lukmanier. The statistics of the ANN output obtained from multi-year time series of nearby weather stations match accurately the ones of the mast data. However, for the rather short validation periods from the LiDAR, the ANN has difficulties in predicting lowest wind speeds at both sites, and highest wind speeds at Les Diablerets.

Keywords Wind energy · Topographic effects · Neural network · Swiss Alps · LiDAR

✉ Fanny Kristianti
fanny.kristianti@epfl.ch

¹ School of Architecture, Civil and Environmental Engineering, Ecole Polytechnique Fédérale de Lausanne (EPFL), Lausanne, Switzerland

² WSL Institute for Snow and Avalanche Research SLF, Davos, Switzerland

³ Department of Atmospheric Sciences, University of Utah, Salt Lake City, UT, USA

1 Introduction

Ongoing climate change with its increasingly severe impacts and negative consequences for the natural and built environment, society, population, and management of natural resources has put a large pressure on implementing sustainable power generation and renewable energy supply systems. Depending on the geographic situation of a region or a country, resources and solutions are seen in solar, wind, hydropower, geothermal, biogas, and other energy production systems. Most of these renewable energy sources are still under-exploited and a large potential for optimized use is seen in most of these domains (Sait et al. 2019). Wind power is one of these with untapped potential, especially in mountain areas (Clifton et al. 2014; Kim et al. 2017).

Following the Fukushima nuclear disaster in 2011, the Federal Department of the Environment, Transport, Energy and Communications (DETEC) of Switzerland has decided to examine the energy strategy for a long-term sustainable energy policy. The Federal Council has developed the 'Energy Strategy 2050' (SFOE 2018) with the strategic objectives to increase energy efficiency, increase the use of renewable energy and reduce nuclear energy. In 2021, a large part of energy for Switzerland is still imported, at approximately 70.3%, and non renewable (Federal Administration of Switzerland, 2021). The non renewable energy sources come from petroleum at one third of total consumption, nuclear energy with one fifth and natural gas with one tenth (Federal Administration of Switzerland, 2021).

Domestically, the energy resources in Switzerland are currently still dominated by hydropower (Federal Administration of Switzerland, 2022). Hydropower provides 62% of domestic electricity production, nuclear 29% and approximately 9% comes from conventional power plants and (new) renewable energy facilities (Federal Administration of Switzerland, 2021). Using hydropower, maximum production occurs during the summer season, due to snow melt and precipitation dynamics (Bavay et al. 2009). However, the energy consumption of Switzerland increases in the winter time for heating and lighting creating a mismatch between consumption and production trends (Dujardin et al. 2017). Therefore, wind power production, which can be enhanced during winter at particular locations, could be a significant contributor to the envisioned mix of renewable energy sources (Dujardin et al. 2021). Also, a general wind speed increase over North and Central Europe during the winter time has been reported by Grams et al. (2017), Clark et al. (2017), Graabak and Korpås (2016) and Archer and Jacobson (2013). This leads to a strong motivation to explore wind power potential to close the seasonality gap.

It is challenging to assess the wind resources in complex terrain, such as the Swiss Alps (Kruyt 2019; Kruyt et al. 2018). We suggest a new methodology, a combination of ground-based remote sensing at a relatively short deployment time with long-term near-surface atmospheric measurements. A light detection and ranging (LiDAR) instrument is chosen because of its ability to measure wind speed over a wide vertical range (Wang et al. 2016) and its simpler deployment compared to a tall mast. While LiDAR remote sensing technology is increasingly used to collect wind speed data, such measurements in complex terrain remain rather challenging. They may be subject to a large bias due to the heterogeneous flow. Assuming horizontal homogeneity, the horizontal velocity measured by the LiDAR may be underestimated by up to 10% in extreme cases (Pitter et al. 2012).

While the interpretation of LiDAR measurements in complex terrain is challenging, a recent publication by Dujardin and Lehning (2022) introduces a deep learning approach (artificial neural network, ANN) to predict wind speed at 10 ms above ground level (a.g.l.) called Wind-Topo. Local topography at a 2-m resolution and the state of the atmosphere

from a numerical weather prediction (NWP) model are used as input. Data from automatic measurement stations are used to calibrate the model, which successfully shows ridge acceleration, sheltering, and deflection mechanisms.

The objective of this study is to propose a method to estimate and assess the wind energy potential in complex terrain by combining LiDAR measurements with meteorological data from spatially distributed weather stations. This novel approach will allow us to generate long-term time series of wind from the relatively short-term LiDAR deployment, under the condition of having a full data set of stations in the vicinity for the long-period target. This method is particularly useful in complex terrain since the wind characteristics vary substantially depending on the location, and it is challenging to have full coverage (no data gaps) from measurement stations.

This paper is organized as follows. Section 2 describes the methods used for wind speed prediction. Note here that the term prediction is not used in the sense of a forecast throughout the paper. It follows the usual terminology in the context of ANN, where the output of an ANN is referred to as a prediction. Details about the measurement campaign locations and data sampling configurations of the instruments are described in Sect. 2.1. The method to generate the time-varying wind speed at a given location, which includes the LiDAR post-processing in combination with the data of the ANN is presented in Sects. 2.2 and 2.3, respectively. Section 3 presents the wind speed characteristics measured by a near-surface ultra-sonic anemometer (Sect. 3.1) and from the LiDAR measurements (Sect. 3.2), and provides a discussion about the ANN prediction of wind potential at the measurement locations (Sect. 3.3). Finally, a discussion of the proposed method and the conclusions from the obtained results are presented in Sect. 4.

2 Methods

2.1 Measurement Station Networks

We use the Inter-Cantonal Measurement and Information System (IMIS, WSL SLF 2022) and SwissMetNet (SMN, MeteoSwiss 2022) networks as shown from Table 1. The IMIS network has 186 measuring stations by 2021. They are distributed throughout the Alpine and Jura areas. An IMIS station consist of snow and wind stations. The purpose of the IMIS network is to provide data for avalanche warnings (Lehning et al. 1999), thus they are mostly located in the mountains at high elevation. SMN stations are used to provide data for weather forecasting in Switzerland. Compared to IMIS, SMN has more stations at middle and low altitudes. IMIS wind speed measurement are conducted at approximately 7.0 m a.g.l. (Lehning et al. 1999) using R.M.Young wind monitor model 05103. SMN wind speed measurements are at 10 m a.g.l. (Kruyt et al. 2022) utilizing Lambrecht L14512 cup anemometers and Thies 2D ultrasonic anemometers (Federal Office of Meteorology and Climatology MeteoSwiss 2023).

2.2 Field Sites and Data Sampling Configuration

The present research is based on two case studies, located in two different regions of the Swiss Alps. The first field campaign was conducted at Lukmanier, on a steep slope west of Piz Scopi, above the Lukmanier Pass, Switzerland, at 2519 m above sea level (a.s.l.) (blue marker, Fig. 1a), from 20 October 2020 to 16 December 2020. The second field campaign

Table 1 Details of weather stations in the proximity of the Lukmanier and Les Diablerets field sites

Station	Region	Lat (N)/Lon (E)	Elev. (m a.s.l.)	Network
<i>Lukmanier area</i>				
COM	Acquarossa/Comprovasco	46°27'34"/8°56'08"	575	SMN
DIS	Disentis	46°42'24"/8°51'12"	1197	SMN
GUE	Gütsch/Andermatt	46°39'09"/8°36'54"	2286	SMN
MTR	Matro	46°25'36"/8°55'29"	2171	SMN
PIO	Piotta	46°30'53"/8°41'17"	990	SMN
SLFDT2	Dötra/Preda	46°32'35"/8°52'08"	2060	IMIS
SLFDTR	Dötra/Costra	46°32'53"/8°51'58"	2391	IMIS
SLFLU2	Lukmanier/Lai Verd	46°36'14"/8°46'59"	2550	IMIS
SLFLUK	Lukmanier/Piz Gannaretsch	46°36'43"/8°47'11"	3040	IMIS
SLFPU2	Puzzetta, Medel/Ilis Plauns	46°37'34"/8°51'45"	2195	IMIS
SLFPUZ	Puzzetta, Medel/La Muota	46°37'22"/8°51'25"	2425	IMIS
<i>Les Diablerets area</i>				
CDM	Col des Mosses	46°23'29"/7°05'54"	1412	SMN
DIA	Les Diablerets	46°19'36"/7°12'14"	2964	SMN
SLFCH2	Chaussy/Pierres Fendues	46°22'36"/7°09'50"	2220	IMIS
SLFCHA	Chaussy/La Para	46°22'58"/7°09'09"	2540	IMIS
SLFCON	Conthey/Etang de Trente Pas	46°17'20"/7°16'31"	2230	IMIS
SLFDIA	Les Diablerets	46°18'51"/7°16'30"	2575	IMIS
SLFFUL	Fully/Grand Chavalard	46°10'43"/7°06'47"	2898	IMIS
SLFLAU	Lauenen/Lauenehore	46°26'25"/7°21'16"	2477	IMIS
SLFNEN	Nendaz/Creppon Blanc	46°08'35"/7°21'15"	2714	IMIS
SLFOBM	Gstaad/Ober Meiel	46°25'18"/7°12'48"	2110	IMIS
SLFVD2	Arbaz, Val. Sionne/Donin du Jour	46°19'15"/7°21'59"	2390	IMIS
SLFVDS	Arbaz, Val. Sionne/Crêta Besse	46°18'19"/7°21'08"	2696	IMIS

was carried out at the Cabane station, Les Diablerets (hereafter Diablerets), at 2523 m a.s.l. (red marker, Fig. 1a) from 20 February 2021 to 2 May 2021. Further details for both campaign locations and measurement statistics can be found in Table 2.

2.2.1 LiDAR Scanning Configuration

During both campaigns, a Halo Photonics Streamline scanning Doppler wind LiDAR (hereafter LiDAR) was deployed. It transmits a laser beam which then is reflected back by aerosols and/or cloud particles. Therefore, the return signal is highly depends on the amount of aerosol available. From that mechanism, we can estimate the radial velocity and derive the wind speed component.

In both campaigns, the LiDAR used 1400 overlapping gates with a range gate length of 30 m, each one shifted by 1.5 m. With this gate overlapping mode, the range of radial wind velocities that can be observed under ideal conditions is 2.1 km. The closest range gates are always contaminated with instrument noise; this range is referred to as blind region. The blind region extends to approximately 60 m from the LiDAR. Gates that fall inside the blind region as illustrated in Fig. 2 are excluded from the analysis. Using the gate overlapping

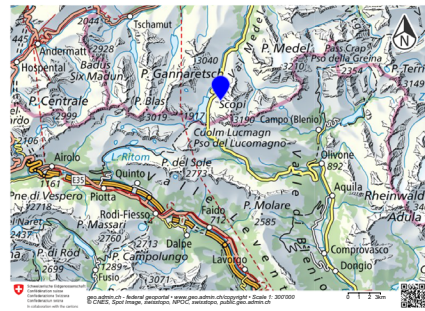
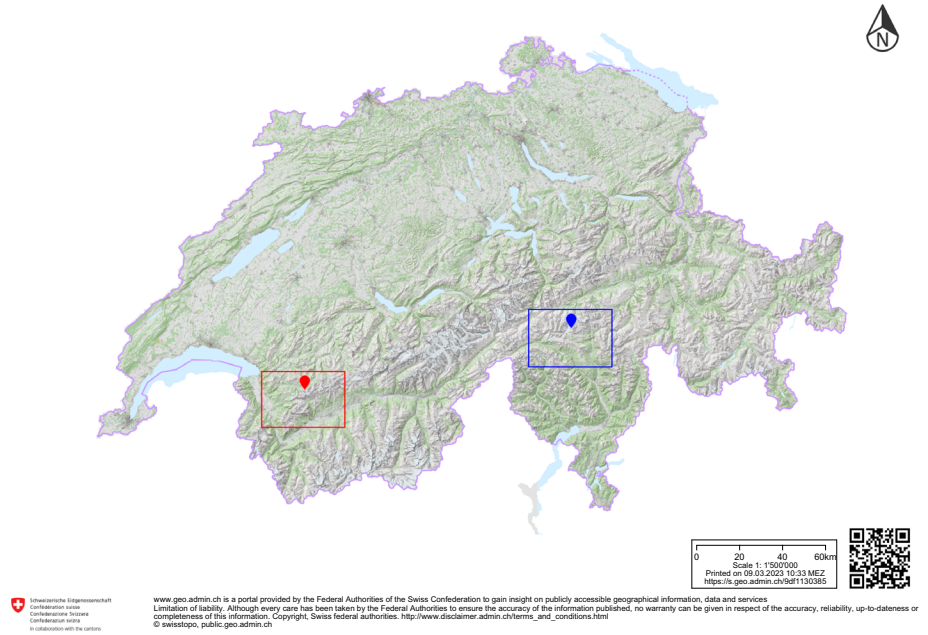


Fig. 1 a Field site locations of the Lukmanier (blue) and Diablerets (red) campaigns. The colored box shows the more detailed topography at Diablerets (b) and Lukmanier (c) campaign sites. Map source: swisstopo (Federal Office of Topography 2023)

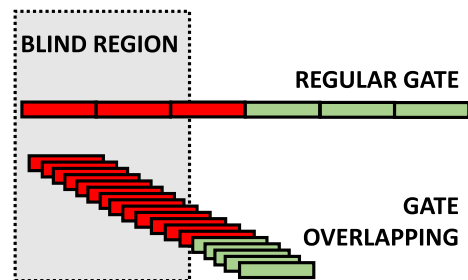
mode reduces the distance between the gate centers compared to the regular sequential gate configuration. This allows for retrieving Doppler wind velocities at a closer distance from the LiDAR (Fig. 2).

At the campaign sites, the LiDAR is set to measure a velocity azimuth display (VAD) wind profile based on a plan position indicator (PPI) scan. During the PPI scan, the elevation angle is fixed. Several scans were performed at the Lukmanier site (see Table 3), but only the 45° elevation angle step stare is used as input for the ANN (see Sect. 2.3). A 6-point step stare PPI scan with equally spaced azimuth directions (VAD6) at 70° is performed on both sites. For PPI step stare, 12 points of 30° azimuth resolution are used. Continuous Scanning Method (CSM) scans yield more data points for the fit, but step stare scans allowed choosing an extended accumulation period, which resulted in stronger returns. Under aerosol-scarce

Table 2 Details about the two field campaigns at Lukmanier and Les Diablerets

Sites	Lukmanier	Les Diablerets
Campaign duration	20/10/2020–16/12/2020	20/02/2021–02/05/2021
LiDAR position	46° 35′ 03″ N / 8° 49′ 08″ E	46° 20′ 24″ N / 7° 12′ 54″ E
CSAT3 height	2.4 m a.g.l.	2.5 m a.g.l.
CSAT3 azimuth	302°	172°
CSAT3 sampling frequency	20 Hz	10 Hz
Elevation	2519 m a.s.l.	2523 m a.s.l.
Max. horizontal wind speed during campaign at 100 m a.g.l. from LiDAR	31.14 m s ⁻¹	29.36 m s ⁻¹
Max. horizontal wind speed during campaign from CSAT3	14.40 m s ⁻¹	18.71 m s ⁻¹
Averaged horizontal wind speed during campaign at 100 m a.g.l. from LiDAR	5.41 m s ⁻¹	4.58 m s ⁻¹
Averaged horizontal wind speed during campaign from CSAT3	3.16 m s ⁻¹	3.08 m s ⁻¹

Fig. 2 Illustration of the LiDAR blind region (gray box) and gate overlap. The gates marked in red cannot be used, while the gates marked in green are outside of the blind region and are reliable. Adapted from HALO (2014)

**Table 3** LiDAR scan sequence at Lukmanier and Les Diablerets site

Sites	Scanning method	Elevation angle (degrees)
Lukmanier	6-point PPI step stare	70
	PPI CSM	27
	12-point PPI step-stare	27 and 45
	PPI CSM	45 and 70
	12-point step-stare PPI	70
Diablerets	6-point PPI step stare	70

conditions, the step-stare mode yielded successful wind retrievals while the CSM scans were not. The scan sequence at the Lukmanier and Diablerets site was repeated every 5 and 10 min respectively.

2.2.2 LiDAR Post-Processing

Raw LiDAR data are filtered and quality controlled to obtain a coherent, high-quality data set. All LiDAR scans, including VAD and PPI, need to pass the quality control described

below. We use several filters during the conversion process of radial velocity V_R into wind speed components u , v and w (Table 4).

The first filter is the blind region filter, which removes the data of the first 60ms of the radial distance. The second filter is the intensity (SNR+1) filter, which removes Doppler velocities with an intensity number < 1.02 . Signal to noise ratio (SNR) refers to the ratio of the mean squared signal to the mean square of the noise. Next, a median to absolute deviation (MAD) filter is used to remove data outside the range of the upper and lower threshold as defined below. This is achieved in several steps: (a) The median of the Doppler velocity at a specific range gate height ($\langle x \rangle$) is calculated. (b) The absolute value of the distance between each data point x_i and the median ($\langle x \rangle$) is calculated. (c) The median of all values calculated in (b) (MAD , see Eq. 1) is calculated. (d) MAD is used to calculate the lower and upper limit of the MAD filter by multiplying MAD with a coefficient (q_{mad}). The coefficient is chosen using a data-driven approach. We tested $q_{MAD} = 7.0$ from Mauder et al. (2013). The value is also chosen as a compromise between the quality and amount of the filtered data. Data points passing this filter need to be larger than the lower limit of MAD and smaller than the upper limit of MAD (Eq. 2):

$$MAD = \langle |x_i - \langle x \rangle| \rangle, \tag{1}$$

$$\langle x \rangle - MAD \cdot q_{MAD} \leq x_i \leq \langle x \rangle + MAD \cdot q_{MAD}. \tag{2}$$

To be able to perform a reliable sine curve fitting (Eq. 5), a filter checking the amount of available data per fit is applied (“Amount of data” filter). The CSM method yields a larger number of data points compared to the step-stare method. Thus, for the CSM method, at least 50% of the data points need to be available to pass this filter. For the step-stare method, a minimum of 8 out of 12 data points is required. For the VAD6 wind profile, which consists of only 6 points per gate, we set the threshold to 5 out of 6 points.

To create a good sinusoidal fitting, in addition to the amount of data, the distribution of data is important. Therefore, we split the data into 6 bins based on the azimuth distribution of VAD6. Each bin consists of 60° azimuth degrees. It is required that all azimuth bins contain at least one data point. An exception is applied to VAD6, due to the limited number of data points. VAD6 is required to fill at least 5 out of 6 bins, following the requirement from the “amount of data” filter.

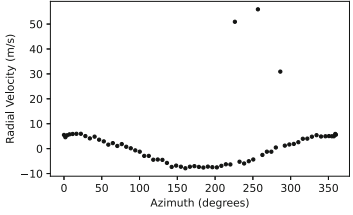
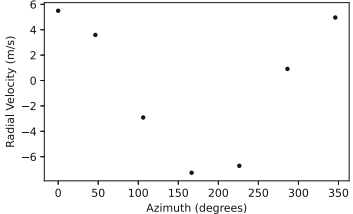
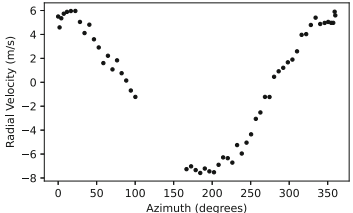
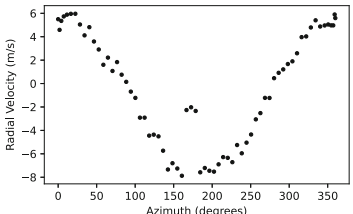
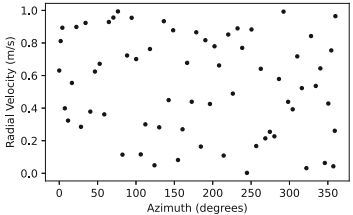
After completing the “amount of data” filter, a first sine curve fitting is performed. We propose the use of an additional partial MAD filter to remove data points with large deviations from the curve fit. We calculate the deviation of the remaining data points x_i to the value which would be expected according to the fitting curve fit_x , instead of the median. Hence, MAD_{part} is the median of the absolute values of the difference of x_i from the fitted curve fit_x (Eq. 3). The upper and lower limit of the partial MAD filter then is determined by multiplying MAD_{part} with q_{MAD} (Eq. 4). We use the same q_{MAD} as the previous filter after checking the effect on our cases. After applying the filter, the retained data then is re-fitted with a new sinus curve:

$$MAD_{part} = \langle |x_i - fit_x| \rangle, \tag{3}$$

$$fit_x - MAD_{part} \cdot q_{MAD} \leq x_i \leq fit_x + MAD_{part} \cdot q_{MAD}. \tag{4}$$

The final filter taking into account the coefficient of determination R^2 shows the quality of the fitted curve (R^2 filter). A minimum R^2 of 0.7 is needed for the radial velocities to be considered valid. Under the assumption of horizontal homogeneity, the data points obtained from the LiDAR measurement should fit into the sinusoidal curve (Eq. 5). A summary of the filters is shown in Table 4, which also includes an example of target case for illustration. We

Table 4 LiDAR data post-processing filters

Filter name	Explanation	Example of target case
Blind region filter	Removal of data within 60 m radial distance from LiDAR	–
Intensity (SNR+1) filter	Removal of data with intensity (SNR+1) < 1.02	–
MAD filter	Removal of data beyond upper and lower limit of MAD filter	
Amount of data filter	Removal of gate height containing less than a specified data limit a. Step-stare mode is limited to at least 8 out of 12 data points b. CSM mode needs to have more than 50% of data compared to the original c. VAD6 only valid if 5 out of 6 data points pass previous filters	
Data distribution filter	a. Step-stare and CSM mode: Remove gate height with empty azimuth bin b. VAD6 is only valid if 5 out of 6 bins are filled with data	
Partial MAD filter	Removal of data beyond upper and lower partial MAD filter	
R ² filter	Removal of wind speed with R ² < 0.7 in the sine curve fitting	

note that this sequential filtering implies a risk of too heavy data manipulation. However, the independent validation of the ANN performance shown below justifies ex-post the choices made.

The percentage of data availability from each filter is shown in Table 5. We use two methods to represent the percentage used: percentage of eliminated data points and percentage of the eliminated gates. The percentage of eliminated data points is used when the filter target the data points, and the other is used when the filter target all data points within one gate. For the data points category, we pick three heights as examples: 100 m a.g.l., 150 m a.g.l., and 200 m a.g.l. for SNR, MAD and MAD_{part} filters. For the eliminated gate category, we calculate the gate up to 200 m a.g.l..

After the filtering process, instantaneous wind vectors composed of the Cartesian components of u , v and w are derived from the instantaneous radial velocity obtained by the PPI LiDAR scans using the VAD retrieval technique and assuming a horizontally homogeneous wind field. Radial wind velocity V_R , as a function of azimuth, follows a sine curve according to Eq. (5) where, θ is the azimuth angle, with zero value at the north direction, and φ is the elevation angle. The wind components u , v , and w are defined as positive when pointing east, north and vertical directions, respectively:

$$V_R = u \sin(\theta) \cos(\varphi) + v \cos(\theta) \cos(\varphi) + w \sin(\varphi). \quad (5)$$

2.2.3 CSAT3

During the Lukmanier field campaign, the Campbell Scientific CSAT3 3-dimensional ultrasonic anemometer (CSAT3) was installed at approximately 4 m horizontal distance south of the LiDAR at 2.4 m above ground. The CSAT3 was facing north-west at 302° azimuth and sampled at 20 Hz. During the Diablerets field campaign, the CSAT3 was installed at approximately 20 m horizontal distance south of the LiDAR at 2.5 m above ground. The CSAT3 was facing south at 172° azimuth and sampled at 10 Hz. In both cases, the CSAT3 was installed over a slight slope, with implications on the vertical wind velocity components (see Sect. 3.1). The CSAT3 orientation was selected based on the expected dominant wind directions. For the Lukmanier site, we chose the direction along the main valley axis and for the Diablerets site the westerly direction. The implementation of the orientation angle is to avoid wind direction from inconvenient angles (i.e. from sectors behind the instrument sampling volume, which may create wakes and disturbances).

2.2.4 Mast

The 25 m height mast measurement was implemented by an external company during the period from October 2011 until April 2016. The mast is located at the middle station of the Stgegia, Piz Scopi ($46^\circ 35' 03'' N / 8^\circ 49' 07'' E$). The wind was measured using R.M. Young Wind Monitor model 05103.

2.3 Temporal Extension of the LiDAR Campaigns with Machine Learning

Long time series of wind speed at the height of a wind turbine hub, typically covering several years, are essential for a reliable assessment of the wind energy potential. The procedure described above provides accurate wind speeds for the duration of the campaign. However, estimating the wind speed for a multi-year period still remains a problem which needs to be addressed.

Table 5 Percentage of the LiDAR data removed by filtering process at Lukmanier and Les Diablerets site

Height Filter name	100 m a.g.l.			150 m a.g.l.			200 m a.g.l.			
	SNR	MAD	MAD_{part}	SNR	MAD	MAD_{part}	SNR	MAD	MAD_{part}	
Percentage of eliminated data points (%) Lukmanier	27 CSM	15.85	15.81	9.47×10^{-3}	12.88	12.84	9.54×10^{-3}	11.89	4.61×10^{-3}	1.21×10^{-1}
	45 CSM	29.92	29.83	2.68×10^{-2}	18.16	18.09	1.72×10^{-2}	14.71	8.83×10^{-1}	5.22×10^{-2}
	70 CSM	35.92	35.81	6.46×10^{-3}	28.20	28.11	2.88×10^{-3}	25.62	9.94×10^{-3}	2.61×10^{-1}
	27 SS	4.53	4.11	1.93×10^{-3}	3.28	3.05	2.10×10^{-3}	2.78	2.84×10^{-3}	1.13×10^{-3}
	45 SS	7.37	6.13	4.78×10^{-3}	4.76	4.41	2.45×10^{-3}	3.68	6.70×10^{-4}	2.08×10^{-3}
	70 SS	5.13	4.65	4.58×10^{-3}	3.59	3.34	3.93×10^{-3}	2.99	3.06×10^{-3}	1.22×10^{-3}
Diablerets	70 VAD	5.33	4.06	5.83×10^{-2}	3.30	2.57	3.38×10^{-2}	2.43	1.52×10^{-2}	3.79×10^{-2}
	70 VAD	3.06	2.96	2.03×10^{-2}	2.10	2.06	6.87×10^{-3}	1.58	3.15×10^{-2}	1.21×10^{-2}
Height	Up to 200m a.g.l.									
Filter name	Data distribution			Amount of data			R^2 filter			
Percentage of eliminated gate (%) Lukmanier	27 CSM	1.01			1.76×10^{-2}			0.14		
	45 CSM	0.89			2.72×10^{-2}			0.15		
	70 CSM	2.16			3.79×10^{-2}			0.29		
	27 SS	6.67			8.10×10^{-3}			0.24		
	45 SS	6.38			8.43×10^{-3}			0.31		
	70 SS	7.18			8.71×10^{-3}			0.26		
Diablerets	70 VAD	14.16			2.50			0.22		
	70 VAD	12.78			7.48×10^{-2}			1.91×10^{-4}		

To assess the wind speed during periods beyond our measuring campaigns we apply an ANN to predict a multi-year time series of wind speed at the two study sites. This method is also known as Measure Correlate Predict (MCP, Jain 2016; Carta et al. 2013). The ANN uses long time series of measurements from surrounding weather stations as inputs (predictors), but not for calibration (predictands). Instead, the LiDAR data is used for calibration. The model then acts as a surrogate for the LiDAR data and models potential LiDAR output (wind speed profile) based on the measurements of the surrounding stations. This way it is possible to obtain a wind speed profile at the location of the LiDAR at any time when the required data from the weather stations is available. This prediction uses the long, multi-year data records of the surrounding automatic weather stations of the Inter-Cantonal Measurement and Information System (IMIS, WSL SLF 2022) and SwissMetNet (SMN, MeteoSwiss 2022) networks. As a first step, suitable stations in the surrounding proximity of the LiDAR location are selected. Details of these stations are summarized in Table 1.

The ANN maps its inputs (station wind speed and height a.g.l. for which a prediction is desired) into the value of wind speed that mimics what the LiDAR would have measured for this particular moment and particular height. By repeating the predictions for a series of heights above ground, a wind speed profile can be generated. This model can be used for any moment when required station data is available as input, hence over multiple years. Prior to training the model, the LiDAR data (wind speeds) generated with the procedure described in Sect. 2.2 passes an additional filter. We only use data points where a valid measurement is available at the range gate above and below it. To make it comparable to the station data, hourly averages of the selected LiDAR data are calculated.

To choose data from the best LiDAR set-up as predictand, the Mean Absolute Error (MAE) value between the prediction and the LiDAR data is continuously monitored during the training and validation process to obtain the lowest possible value. Based on this selection process, for the Lukmanier site, the wind speed profile from the 45° elevation angle step-stare method is chosen to train the ANN. For the Diablerets site, the 6-point step stare PPI at 70° elevation angle is used. To allow for training and validation, we split the LiDAR data into 10 periods. The first 80% of each period is used to train the model and the last 20% of each period is used for validation. Furthermore, as events with high wind speed are rather rare and not necessarily well distributed between the training and validation sets, a random selection of 80% of the moments with a wind speed larger than 7 m s^{-1} is placed in the training set, while the remaining 20% are placed in the validation set. From this process, we obtain for the Diablerets and Lukmanier sites 201 and 88 h of validation data, respectively, selected from the LiDAR data with 1728 and 1392 hourly averages, respectively.

The ANN is composed of four hidden layers with 32, 16, 8, and 4 neurons respectively. The activation functions of Continuously Differentiable Exponential Linear Units (CELU, Barron (2017)) can be expressed by $CELU(x) = \max(0, x) + \min(0, \exp(x) - 1)$. The loss function \mathcal{L} (Eq. 6) is the mean squared error (MSE) scaled by the inverse of the probability of occurrence of the targeted wind speed: Data with high wind speed, which occurs less often, are given more importance in the loss function. This adaptation of the MSE was critical to obtaining correct distributions of wind speed:

$$\mathcal{L} = \frac{1}{N} \sum_{i=1}^N \frac{(\hat{y}_i - y_i)^2}{0.01 + P(y_i)}, \quad (6)$$

where \hat{y}_i is the predicted wind speed, y_i is the measured wind speed, $P(y_i)$ is the probability of y_i being in the training set and N is the batch size used for training. The model is trained using the ADAM optimizer with a learning rate of 10^{-4} and a batch size of 32. Convergence

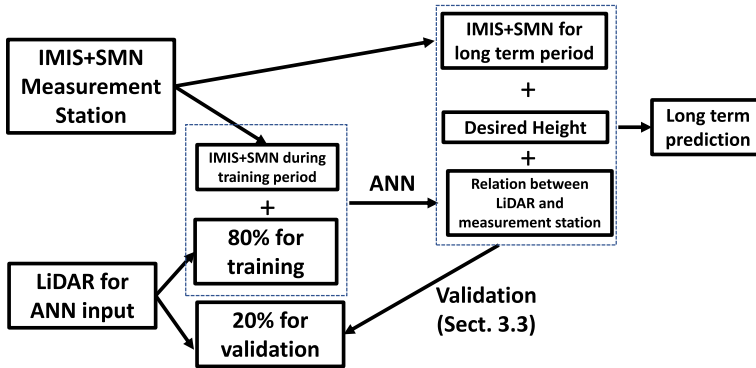


Fig. 3 Flowchart of temporal extension of LiDAR campaign with Machine Learning

is reached after a dozen of epochs. For the multi-year prediction of wind speeds with the ANN, measurements of 12, and 11 stations in the surroundings of Diablerets, and Lukmanier, respectively, are collected (Table 1). It is necessary to have a complete set of input data for all stations to generate a prediction with the ANN. Therefore, we need to eliminate periods of one or more empty data values from the station data sets. The availability of data determines the duration of the target predictions, ideally as long as possible. The validation process using the validation period of the LiDAR data for both field sites is further described in Sect. 3.3. Summary of Sect. 2.3 can be seen in Fig. 3.

3 Results and Discussion

3.1 Near-Surface Measurements

In this section, characteristics of local near-surface wind measurements from the 3-D ultrasonic anemometer (CSAT3) are presented. Given their lower measurement height compared to the LiDAR measurements, data from the CSAT3 are more suitable to represent the near-ground situation at the campaign sites.

Figure 1b shows the topographical situation at the Lukmanier site. The main wind directions at the Lukmanier site during the campaign period, measured by the CSAT3, range from north-east to south-east (Fig. 4). The horizontal and vertical wind speed distribution during the Lukmanier campaign can be seen in Fig. 5a, b respectively. The largest values of the vertical wind speed are associated with the sector 90° – 180° (Fig. 5e, green and red color), which occurs in combination with the majority of high horizontal wind speed from the south-easterly sector (Fig. 4). This could be with the synoptic wind coming from southerly directions which is influenced by Piz Vallatscha and forced to move parallel to the terrain contour lines (Fig. 1b). Vertical wind speed components are mostly negative at the measurement location (Figs. 1b and 5c). The negative vertical wind component at Lukmanier is interpreted as a result of a superposed downslope wind component from Piz Vallatscha, located east of the measurement site, similar to a katabatic wind.

Figure 5e shows the correlation between the vertical and horizontal wind speed components. The different correlations indicate different characteristics for the three wind direction sectors: 0° – 90° (blue and orange dots), 90° – 180° (green and red dots), and 270° – 360° (pink

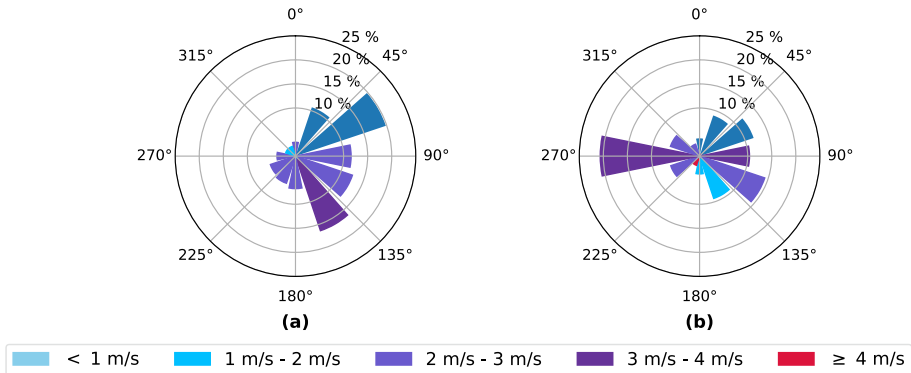


Fig. 4 Wind roses based on CSAT3 measurements **a** at the Lukmanier site between 20/10/2020 and 16/12/2020 and **b** at the Diablerets site between 20/02/2021 and 02/05/2021. The average horizontal wind speed per azimuth sector is shown in color

and light green dots). The three observed regimes can be associated with the local topography around the measurement site. The first regime of near-zero vertical velocity includes winds from sectors 0° – 90° where horizontal wind velocities cover a wide range of wind speeds compared to the vertical velocities. These characteristics are related to the wind blowing parallel to the contour lines of Piz Vallatscha. The second regime includes winds from sectors 90° – 180° , where the vertical wind component becomes more negative for increasing horizontal wind speed. This sector comprises strongly deviated synoptic winds from southerly or south-westerly, as well as katabatic winds down the western slope of Piz Vallatscha (see map in Fig. 1b). The third regime including sectors 270° – 360° features positive vertical wind speed components at rather moderate horizontal velocity, compared to the other two regimes. This regime represents the synoptic and valley winds from a north-westerly direction, which are forced up-slope due to the orographic obstacle.

The three regimes are also visible in the form of a quasi-sinusoidal pattern when vertical wind speed is plotted against the wind direction (Fig. 5g). The light blue color represents the wind speed during the daytime of 0900 UTC+1–2100 UTC+1 and the purple color represents the wind speed during the nighttime of 2100 UTC+1–0900 UTC+1. Separating the diurnal cycle in a daytime and nighttime period shows, in general, a slight increase in the amplitude of the vertical wind speed component during the day. This underlines the strong diurnal effect at the Lukmanier site, especially for a wind direction of 100° – 200° .

Figures 1c show the terrain situation at the Diablerets site. The data were collected during a 2.5 months period in spring 2021. According to the CSAT3-based wind rose (Fig. 4), the main wind direction at the Diablerets site is from the west. Secondary dominant wind directions are north-easterly to south-easterly winds. The westerly wind is the terrain-influenced synoptic flow coming from the wide-open area of Lake Geneva. The flow is then channeled through the Ormont valley and experiences a strong orographic lifting when it reaches Diablerets mountain massif. Figure 5b, d show the time series of the horizontal and vertical wind speed components, respectively, during the campaign period. The mean horizontal wind speed is 3.08 m s^{-1} . The maximum horizontal and vertical wind speeds are aligned with the main wind directions (Fig. 4). From 20 to 22 March 2021, a strong wind event is apparent in the vertical and horizontal wind velocity measurements (Fig. 5b) from the west sector (pink and brown color, Fig. 5d).

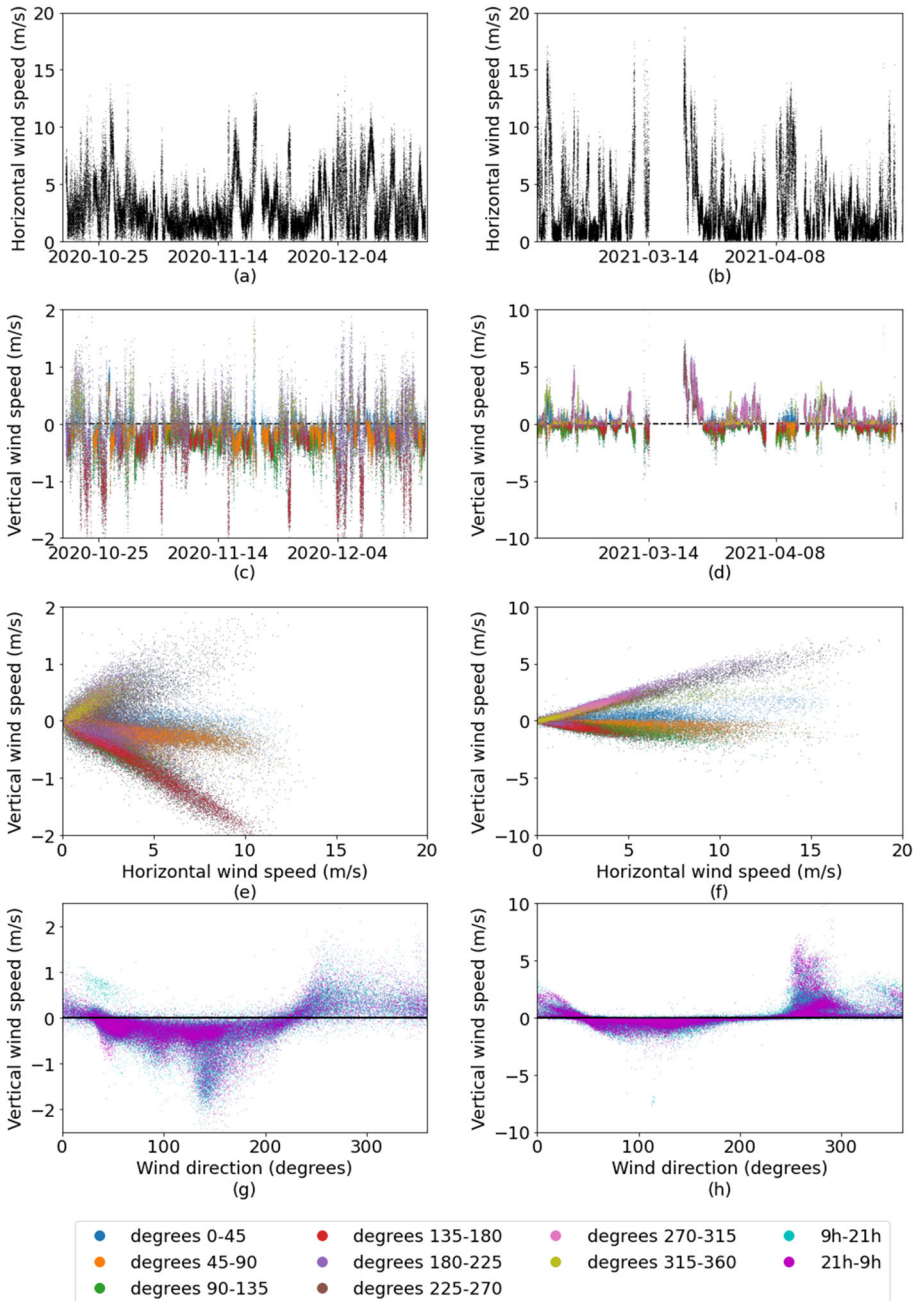


Fig. 5 Measurements of the CSAT3 3-D ultra-sonic anemometer at the Lukmanier (20/10/2020–16/12/2020, left panel) and Diablerets (20/02/2021–02/05/2021, right panel) sites. **a** Horizontal and **c** vertical wind speed, **e** correlation of horizontal and vertical wind speed, and **g** correlation of vertical wind speed and wind direction at the Lukmanier site. **b** Horizontal and **d** vertical wind speed, **f** correlation of horizontal and vertical wind speed, and **h** correlation of vertical wind speed and wind direction at the Diablerets site. Wind direction is color-coded sector-wise, and day/night periods are marked blue and red, respectively

The correlation between vertical and horizontal wind speed is shown in Fig. 5f. Positive vertical wind components are strongly increasing with the increase of wind speed for the wind direction sector 270° – 360° (pink and light green dots) over a wide range of wind speeds. The other sectors show only moderate vertical components: N to NE slightly positive (blue dots), NE to SE slightly negative but for strong winds (orange and green dots), SE to S slightly negative at weaker winds (red dots). Winds with a positive vertical component are mostly from 225° to 360° , i.e. SW to N (Fig. 5h), which is coherent with the impact of the orographic obstacle (Fig. 1c). Winds with a negative vertical component are occupying the remaining sectors from 45° to 225° , i.e. NE to SW (Fig. 5h), again coherent with the sloping terrain. Southerly winds may have two different origins: (a) strong Foehn winds crossing the Diablerets mountain massif, and (b) cold katabatic winds draining the Zanfleuron glacier (see Fig. 1c).

Overall, from both sites, we see a strong terrain effect in the near ground measurement data. The wind local characteristics are also strongly influenced by the interplay between the synoptic wind and the local terrain. Thus, it is important to consider both the local terrain and synoptic scale wind when assessing the wind energy potential at a given site.

3.2 Characteristics of Local Wind Flow Above the Ground

To harvest the wind energy potential, we also need to study the wind flow at a typical operating height of wind turbines. In this section, we will discuss the local wind characteristics measured by the LiDAR at altitude levels higher above the ground. By comparing the local wind characteristics at the study sites from both the near-surface measurements (Sect. 3.1) and the measurements at the operating height of a wind turbine (Sect. 3.2), the characteristics of wind flow can be summarized.

For the Lukmanier site at 100 m a.g.l., the horizontal wind speed statistics show an average wind speed of 5.41 m s^{-1} , which is higher than the near-surface measurement of 3.16 m s^{-1} . The maximum wind speed is 31.14 m s^{-1} coming from the direction of 158° on 5 December 2020. This agrees with the event of maximum wind measured by the CSAT3 near the ground. Figure 6 shows the wind rose at various heights above ground level obtained from LiDAR measurements (left), the Consortium for Small-scale Modeling (COSMO-1) analysis (middle), and the Wind Atlas Switzerland (right, Koller and Humar 2016). COSMO-1 is available at 1.1 km resolution in hourly intervals and covers the entire area of Switzerland. The Wind Atlas of Switzerland provides the average annual wind speed at several heights above ground level in 100 m horizontal resolution. From the LiDAR measurements, we see that the major wind direction at the Lukmanier site is more concentrated in the north to north-eastern and the southern sectors, compared to results from the CSAT3 measurements (Fig. 4). The concentrated wind direction from the LiDAR is likely the synoptic wind that is following the main valley axis and is less influenced by katabatic effects. With increasing altitude, wind from the southern sector is also becoming more frequent. This could be due to the mountain range to the south of the Lukmanier site (Pizzo del Sole, Pizzo d’Era and Pizzo di Campello) (Fig. 1b), which obstructs the southerly flow at lower altitude. The campaign site is located at 2519 m a.s.l., while the highest point of Pizzo del Sole is 2773 m a.s.l. The height difference could explain the obstruction of the southerly wind that comes from Valle Leventina.

COSMO-1 analysis (Fig. 6, second column) identifies the southerly sectors as the main wind direction during the campaign period. Taking a closer look into the terrain situation (Fig. 1b), it is likely that the southerly wind from Valle Leventina moves over the mountain ridge of Pizzo del Sole and then turns to the north in the direction of Val Medel. This is

in agreement with high wind speeds from the southern direction by COSMO-1. However, COSMO-1 seems to be unable to represent the interplay between katabatic flow from the ridge of Piz Scopi, Piz Miez, and Piz Vallatscha, which is prevalent in the near-surface CSAT3 measurements, with the synoptic wind blowing through Val Medel. Therefore, we cannot see the high northerly to north-easterly wind speeds at the lower elevation levels in the COSMO-1 analysis. Another reason could be the coarse COSMO-1 resolution, which is not able to resolve the detailed terrain structures and hence its effect on small-scale wind patterns.

The Wind Atlas Switzerland, on the other hand, shows high wind speeds coming from the northern sector. The absence of the increasing southerly wind with height (as seen from the LiDAR and COSMO-1 wind roses) suggests that Wind Atlas Switzerland may not capture the flow effects created by blockage from the ridge of Pizzo del Sole. However, this is a speculative explanation because the differences between the wind roses may also be explained by the fact that the Wind Atlas Switzerland represents the annual mean while the CSAT3 and LiDAR measurements represent the wind conditions during the winter campaigns. It is possible that the other seasons involve other wind flow mechanisms, which are not well represented by the short term LiDAR measurements and COSMO simulation.

For Diablerets, the wind rose from the LiDAR measurements, the COSMO-1 analysis, and the Wind Atlas Switzerland show a similar tendency of main wind direction from the north-eastern and south-western sectors (Fig. 7). A less frequent but strong wind from the south is also observed in the LiDAR measurements and in the COSMO-1 analysis. At higher levels, we further see a more prominent wind speed coming from the north-eastern sector, compared to the more varying wind directions measured by the CSAT3. This could be due to the weaker katabatic effect of the Oldehore peak compared to what we see from the near-surface measurements, similar to the mechanism discussed for the Lukmanier site (Sect. 3.1). This interplay between katabatic flow and wind forced dynamically by the main terrain topography is causing the upper-level wind to show a distribution peak in the north-east direction, along the main axis of the Ormont valley.

Overall, at the Lukmanier site, we see different wind roses during the campaign period (from LiDAR and COSMO-1) and annual period (from the Wind Atlas Switzerland). One of the reasons could be that the flow effect caused by blockage from Pizzo del Sole is not represented well in the Wind Atlas Switzerland. Another reason is that there are other seasonal wind flow mechanisms which are not well represented during the campaign period. For Diablerets site, however, we see a good agreement between the wind roses from the campaign period and the annual period. This might suggest that the wind rose that we obtained during the short term campaign is relatively representative of the annual mean in Diablerets. Even if the wind flow mechanisms are expected to change with season, the terrain channeling effect in Diablerets leads to similar wind patterns throughout the year, thus the similar shape of wind rose. For both study sites (Lukmanier and Diablerets) a similar range of average and maximum wind speeds are observed, even though the two sites are far apart, located in the eastern and western parts of Switzerland, featuring different situations of complex topography. These similar statistics could be explained by the similar elevation above sea level (Table 2), therefore making both sites influenced by similar synoptic scale wind. The shift in wind direction between LiDAR and CSAT3 measurements shows that close to the surface terrain effects, such as katabatic flows, play an important role. At a higher levels, where wind turbines operate, the larger scale topographic features, such as the valley orientation, play a more important role. The shift between the principal wind flow near the surface and further aloft needs to be put into consideration in the planning process of harvesting wind energy in complex terrain.

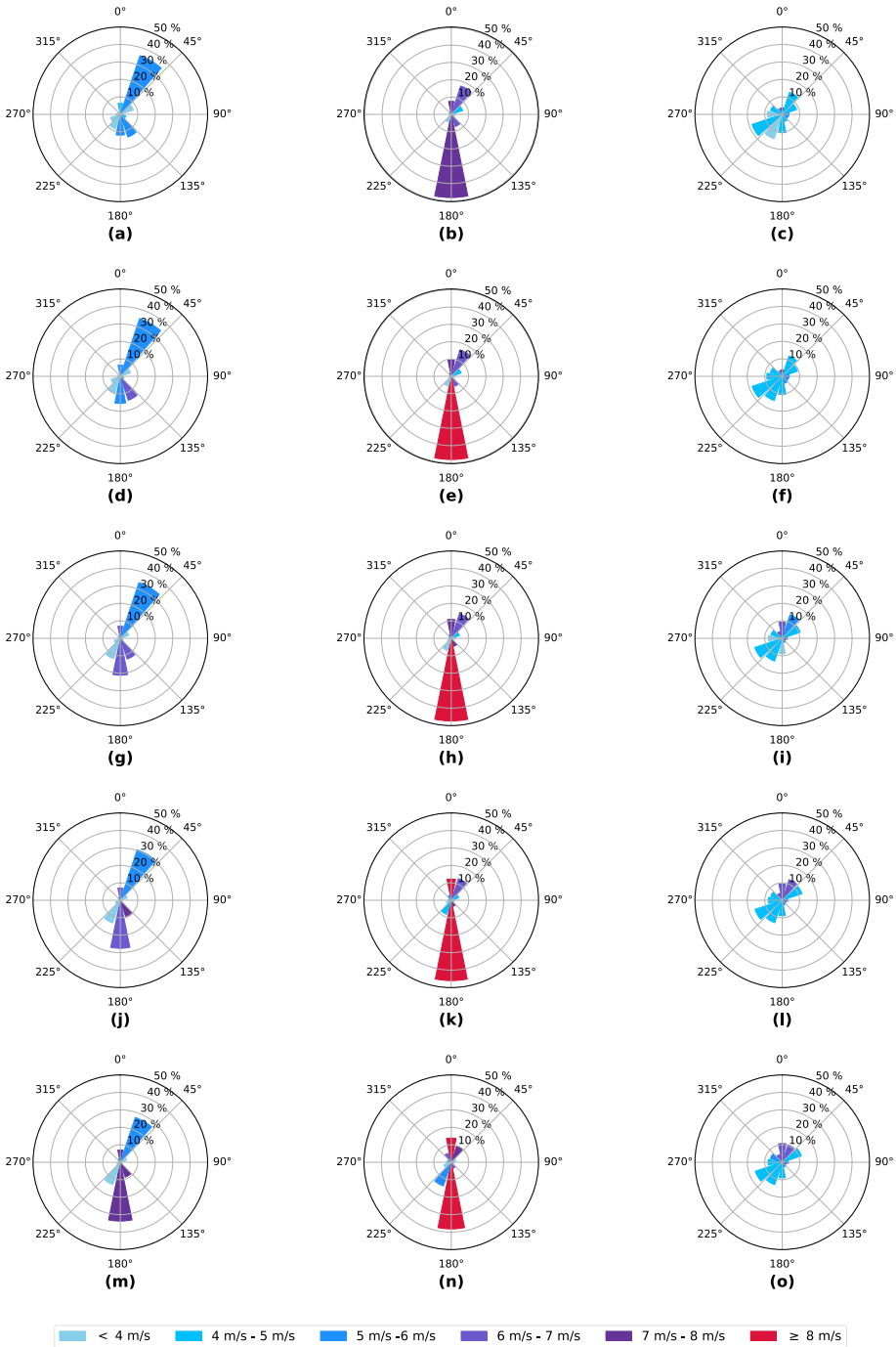


Fig. 6 Wind roses at the Lukmanier site based on LiDAR measurements from 20/10/2020 to 16/12/2020 (left column), COSMO-1 from 20/10/2020 to 16/12/2020 (middle column), and the Wind Atlas Switzerland (right column) for a one-year duration. The elevation levels are 50 m, 75 m, 100 m, 125 m, and 150 m a.g.l. for each row, respectively. The average horizontal wind speed per azimuth sector is shown in color

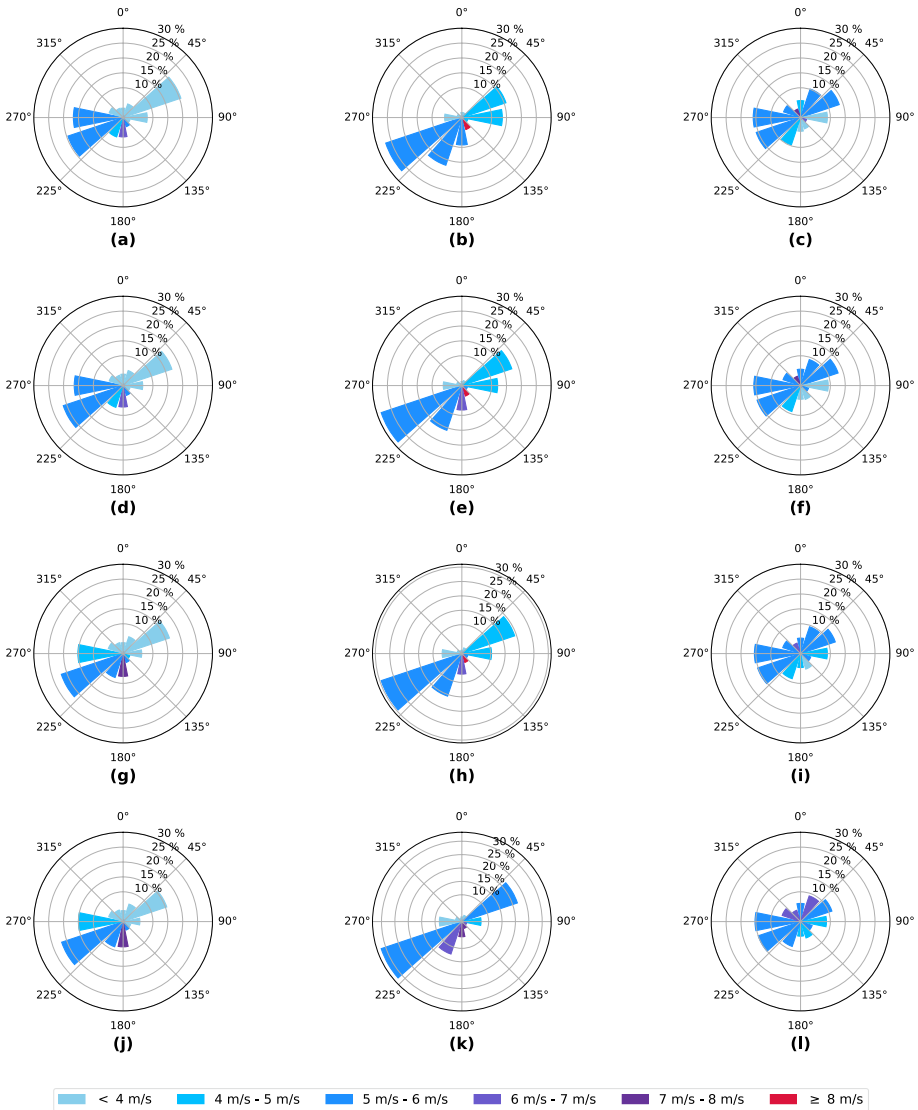


Fig. 7 Wind roses at the Diablerets site based on LiDAR measurements from 20/02/2020 to 02/05/2021 (left column), COSMO-1 from 20/10/2020 to 16/12/2020 (middle column), and the Wind Atlas Switzerland (right column) for a one-year duration. The elevation levels are 75 m, 100 m, 125 m, and 150 m a.g.l. for each row, respectively. The average horizontal wind speed per azimuth sector is shown in color

3.3 Wind Speed Prediction by Machine Learning

The spatial and temporal variation of wind speed throughout the year also needs to be considered, therefore a long-term time series of wind speed is needed for planning purposes. For each study site, the ANN is used to predict time series of wind speed at various heights above ground as long as the input data set is available. At the Lukmanier site, we check the model performance during the validation period and with measurements from the mast. Figure 8a

shows the averaged result of the predicted wind speed profile at the LiDAR site during the mast measurement period. It shows an increasing trend of wind speed with height (black line). This predicted profile also perfectly coincides with the average wind speed measured by the mast (red star). Figure 8d shows a quantile–quantile plot to compare the data distributions by their quantile values during the mast measurement period. The dark line shows the theoretical expectation for a perfect model and the red dots show the actual prediction from the ANN. Between 1 m s^{-1} and 5 m s^{-1} , the ANN slightly underestimates the wind speed. For the first quantile, the ANN predicts some negative wind speed values, which indicates that the model did not get sufficient low wind speed data during the training and therefore extrapolates poorly for low wind speed. For the rest of the analysis, negative values are replaced by zero. Figure 8e shows the histogram of wind speed from the mast (black) and ANN (red) at 25 m a.g.l. during the mast measurement period. A Weibull distribution is then fitted for both mast (green cross) and ANN (blue line). A good match of the Weibull fits from the ANN prediction (and the mast measurements) can be seen. From the histogram, we also see the underestimation tendency at the low wind speed that we observed in the quantile–quantile plot.

At the Lukmanier site, during the validation period, the ANN predicts a vertical profile with higher wind speed than what the LiDAR measured (Fig. 8b). The vertical profile from the LiDAR is constructed by taking the mean value of all available data, gate-wise. This explains its non-smoothness, which is the result of all the data gaps. For the ANN, which can produce data without gaps, a smooth profile (black) is generated, which contains also data from range gates, where the LiDAR has no data. Therefore, for better comparison, we generate another profile (blue) by excluding data from the ANN where the LiDAR had gaps. It is worth noticing that despite its overestimation, the ANN reproduces well the shape of the vertical profile. The aforementioned overestimation is due to the incapacity of the ANN to predict some very low wind speeds during the validation period. Figure 8f depicts the distributions of wind speed from LiDAR and ANN during the validation period and illustrates this problem clearly. Compared to the histogram from the long mast period (Fig. 8e), the histogram from the short validation period is less smooth. This is due to the small amount of data available. From the mast measurement, we obtained approximately 9890 h of data for comparison. For the validation period, we compare only 88 and 201 hourly data for Lukmanier and Diablerets sites, respectively. At Diablerets, Fig. 8c shows that here ANN underestimates the wind speed compared to the LiDAR measurement. From the histogram in Fig. 8g, we see that the ANN has the same difficulty of predicting low wind speed events during the validation period at Diablerets. In addition, it does not predict any wind speed larger than 12 m s^{-1} . While the ANN was able to predict high wind speed at Lukmanier, we can speculate that the more complex topography of Diablerets, leading to highly sheared and temporally varying wind profiles, is the reason for the lower performance at this site.

Figure 9 shows the distributions of wind speed predicted by the ANN for the long-term period at various levels for Lukmanier (left column) and Diablerets (right column). The long-term predictions for Lukmanier cover 20 October 2016–18 December 2020. 22% of the original data was removed due to the unavailability of one or more of the stations. For Diablerets, 19.5% of the data from the period of 12 April 2018–2 May 2021 had to be removed because of missing values. A summary of the mean wind speed from LiDAR measurements, the Wind Atlas Switzerland, and the long-term ANN predictions are given in Table 6. Overall, at Lukmanier, the average wind speeds from Wind Atlas Switzerland and from the ANN are in good agreement. For Diablerets site, the ANN prediction is shifted towards lower wind speeds compared to the Wind Atlas Switzerland, which results in a lower mean wind speed (Fig. 9).

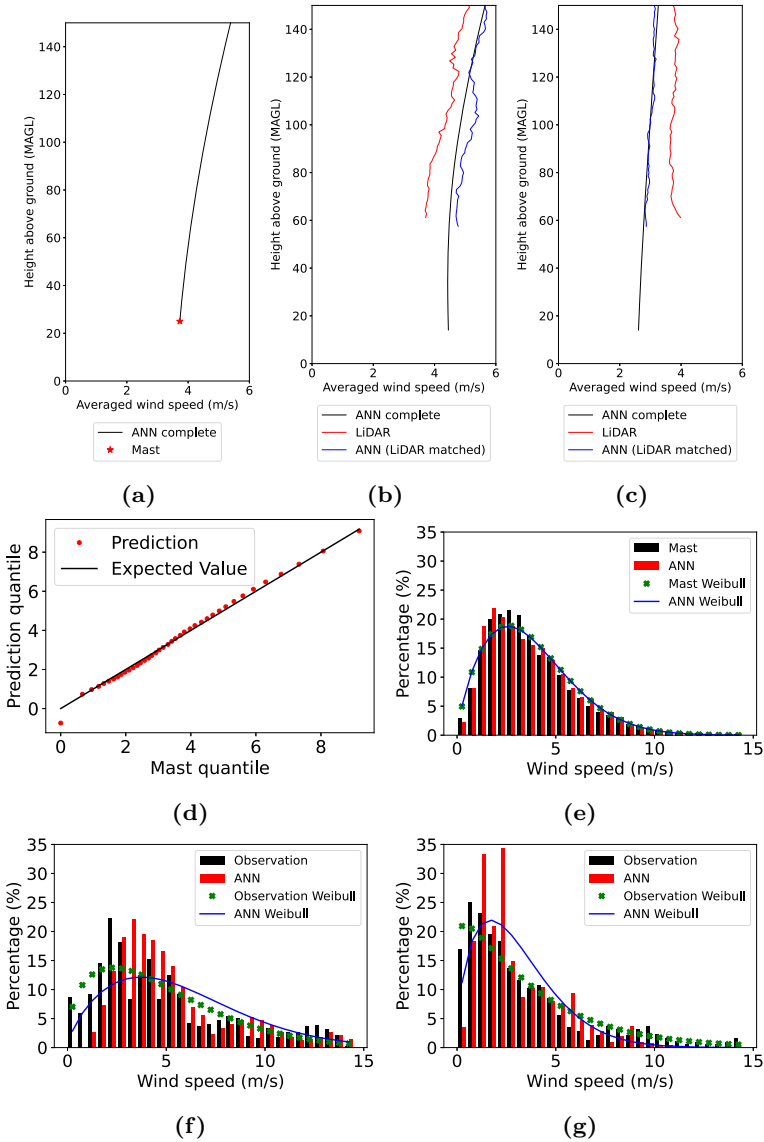


Fig. 8 a Average wind speed profile from ANN at the Lukmanier site for the period of mast measurements from October 2011 until April 2016. The red star shows the average wind speed from the mast at 25 m a.g.l. Mean wind speed profile from ANN at b Lukmanier and c Les Diablerets during the validation period. The red, black, and blue lines show the LiDAR measurements, the ANN, and the ANN with data gaps as in the LiDAR data, respectively. d Quantile–Quantile plot from the Lukmanier site for the period of mast measurements. Red dots show the prediction and the black line shows the expected values. Weibull distribution of wind speed at the Lukmanier site during e the mast measurement period, f the validation period, and g at the Les Diablerets site during the validation period. Red colored bars show the predicted values and black bars show observation values from the mast at 25 m a.g.l. and LiDAR at 75–150 m a.g.l. The blue line shows the Weibull fit for the prediction value and the green dots show the Weibull fit for the mast and LiDAR

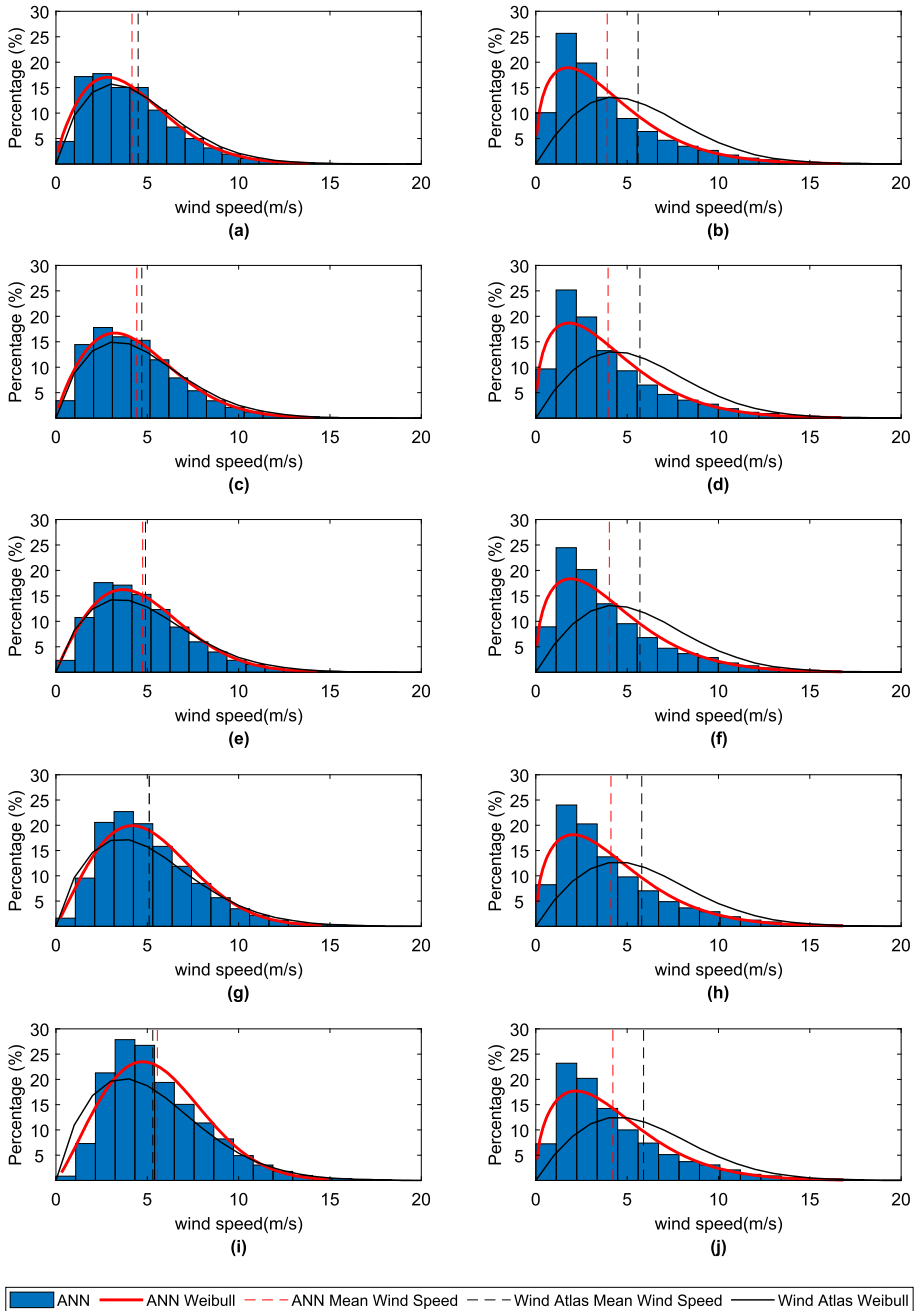


Fig. 9 Histograms of wind speed based on the long-term ANN predictions at Lukmanier (20/10/2016–18/12/2020, left) and Les Diablerets (12/04/2018–02/05/2021, right), respectively, at **a, b** 50 m a.g.l., **c, d** 75 m a.g.l., **e, f** 100 m a.g.l., **g, h** 125 m a.g.l. and **i, j** 150 m a.g.l. Weibull distributions are shown for the ANN prediction (red line) and for the Wind Atlas Switzerland (black line). The dashed lines show the average wind speed from Wind Atlas Switzerland (black) and the ANN prediction (red)

Table 6 Comparison of mean wind speed at different heights above ground between the LiDAR measurements during the campaign period, the Wind Atlas Switzerland for annual average values, and ANN prediction for long-term period results

Height (m a.g.l.)	Mean wind speed from LiDAR during campaign (m s^{-1})	Mean wind speed from wind atlas Switzerland (m s^{-1})	Mean wind speed from ANN for long term period (m s^{-1})
<i>Lukmanier</i>			
50	4.6	4.5	4.2
75	5.0	4.7	4.4
100	5.0	4.9	4.7
125	5.4	5.1	5.1
150	5.9	5.3	5.6
<i>Les Diablerets</i>			
50	–	5.6	3.9
75	4.5	5.7	4.0
100	4.6	5.7	4.0
125	4.6	5.8	4.1
150	4.7	5.9	4.2

4 Conclusions

The wind energy assessment process in complex terrain remains a challenging process. Using the combination of data from two field campaigns in the Alpine region of Switzerland and including near-surface CSAT3 and higher altitude LiDAR measurements, we are able to obtain both a general overview and a detailed understanding of the local wind dynamics. It is important to take into account the interplay between katabatic, anabatic and terrain-influenced synoptic winds at various height levels. Wind potential was investigated by combining data from two field campaigns and from long-term measurements of surrounding weather stations using an artificial neural network (ANN). The result from this technique has shown a very good agreement with data obtained at a 25 m tall mast at the Lukmanier site. While long-term statistics are well reproduced by the ANN at Lukmanier site, results on shorter time scales show that additional data from longer LiDAR measurement campaigns could be beneficial. The difficulties of the ANN in predicting low or high wind speed events could be alleviated with more training data. The good agreement between the shapes of the measured and predicted vertical profiles of wind speed indicates that this new ANN technique is a promising tool for assessing wind power potential in mountainous areas and particularly in complex terrain.

Acknowledgements We thank Glacier3000, Planair, Meteo Swiss, Swiss Federal Department of Defence, Civil Protection and Sport, and Halo Photonics online support for data provisions, collaborations and supporting the field campaign. This research published in this report was carried out with the support from the Swiss National Science Foundation (SNSF): Grant 200020_179130, Swiss Federal Office of Energy (SFOE): MaxWEP, Swiss Federal Office of Energy (SFOE): SWEET EDGE and from the Swiss National Supercomputing Centre (CSCS) projects s938 and s1115.

Funding Open access funding provided by EPFL Lausanne

Open Access This article is licensed under a Creative Commons Attribution 4.0 International License, which permits use, sharing, adaptation, distribution and reproduction in any medium or format, as long as you give

appropriate credit to the original author(s) and the source, provide a link to the Creative Commons licence, and indicate if changes were made. The images or other third party material in this article are included in the article's Creative Commons licence, unless indicated otherwise in a credit line to the material. If material is not included in the article's Creative Commons licence and your intended use is not permitted by statutory regulation or exceeds the permitted use, you will need to obtain permission directly from the copyright holder. To view a copy of this licence, visit <http://creativecommons.org/licenses/by/4.0/>.

References

- Archer CL, Jacobson MZ (2013) Geographical and seasonal variability of the global “practical” wind resources. *Appl Geogr* 45:119–130. <https://doi.org/10.1016/j.apgeog.2013.07.006>
- Barron JT (2017) Continuously differentiable exponential linear units. <https://doi.org/10.48550/ARXIV.1704.07483>
- Bavay M, Lehning M, Jonas T, Löwe H (2009) Simulations of future snow cover and discharge in alpine headwater catchments. *Hydrol Process* 23(1):95–108. <https://doi.org/10.1002/hyp.7195>
- Carta JA, Velázquez S, Cabrera P (2013) A review of measure-correlate-predict (MCP) methods used to estimate long-term wind characteristics at a target site. *Renew Sustain Energy Rev* 27(C):362–400. <https://doi.org/10.1016/j.rser.2013.07.000>
- Clark RT, Bett PE, Thornton HE, Scaife AA (2017) Skilful seasonal predictions for the European energy industry. *Environ Res Lett* 12(2):024002. <https://doi.org/10.1088/1748-9326/aa57ab>
- Clifton A, Daniels MH, Lehning M (2014) Effect of winds in a mountain pass on turbine performance. *Wind Energy* 17(10):1543–1562. <https://doi.org/10.1002/we.1650>
- Dujardin J, Lehning M (2022) Wind-topo: Downscaling near-surface wind fields to high-resolution topography in highly complex terrain with deep learning. *Q J R Meteorol Soc* 148(744):1368–1388. <https://doi.org/10.1002/qj.4265>
- Dujardin J, Kahl A, Kruyt B, Bartlett S, Lehning M (2017) Interplay between photovoltaic, wind energy and storage hydropower in a fully renewable Switzerland. *Energy* 135:513–525. <https://doi.org/10.1016/j.energy.2017.06.092>
- Dujardin J, Kahl A, Lehning M (2021) Synergistic optimization of renewable energy installations through evolution strategy. *Environ Res Lett* 16(6):064016. <https://doi.org/10.1088/1748-9326/abfc75>
- Federal Office of Meteorology and Climatology MeteoSwiss (2023) Measurement instruments. <https://www.meteoswiss.admin.ch/weather/measurement-systems/land-based-stations/automatic-measurement-network/measurement-instruments.html>. Accessed 9 Feb 2023
- Federal Office of Topography (2023) Swiss map raster. <https://map.geo.admin.ch/>. Accessed 11 March 2023
- Graabak I, Korpås M (2016) Variability characteristics of European wind and solar power resources—a review. *Energies*. <https://doi.org/10.3390/en9060449>
- Grams CM, Beerli R, Pfenninger S, Staffell I, Wernli H (2017) Balancing Europe’s wind-power output through spatial deployment informed by weather regimes. *Nat Clim Chang* 7(8):557–562
- HALO (2014) Halo photonics stream line scanning doppler lidar system - v14 software guide. Tech rep., HALO Photonics
- Jain P (2016) Wind energy engineering. McGraw-Hill Education
- Kim HG, Kang YH, Kim JY (2017) Evaluation of wind resource potential in mountainous region considering morphometric terrain characteristics. *Wind Eng* 41(2):114–123
- Koller S, Humar T (2016) Windpotentialanalyse für windatlas.ch: Jahresmittelwerte der modellierten windgeschwindigkeit und windrichtung
- Kruyt AC (2019) Potential and uncertainty of wind energy in the swiss alps. EPFL thesis, p 126. <https://doi.org/10.5075/epfl-thesis-9350>
- Kruyt B, Dujardin J, Lehning M (2018) Improvement of wind power assessment in complex terrain: the case of COSMO-1 in the Swiss Alps. *Front Energy Res* 6:102. <https://doi.org/10.3389/fenrg.2018.00102>
- Kruyt B, Mott R, Fiddes J, Gerber F, Sharma V, Reynolds D (2022) A downscaling intercomparison study: the representation of slope- and ridge-scale processes in models of different complexity. *Front Earth Sci*. <https://doi.org/10.3389/feart.2022.789332>
- Lehning M, Bartelt P, Brown B, Russi T, Stöckli U, Zimmerli M (1999) snowpack model calculations for avalanche warning based upon a new network of weather and snow stations. *Cold Reg Sci Technol* 30(1):145–157. [https://doi.org/10.1016/S0165-232X\(99\)00022-1](https://doi.org/10.1016/S0165-232X(99)00022-1)
- Mauder M, Cuntz M, Drüe C, Graf A, Rebmann C, Schmid HP, Schmidt M, Steinbrecher R (2013) A strategy for quality and uncertainty assessment of long-term eddy-covariance measurements. *Agric For Meteorol* 169:122–135. <https://doi.org/10.1016/j.agrformet.2012.09.006>

- MeteoSwiss (2022) Meteoswiss idaweb. <https://gate.meteoswiss.ch/idaweb/>. Accessed 2022
- Pitter M, Abiven C, Vogstad K, Harris M, Barker W, Brady O (2012) Lidar and computational fluid dynamics for resource assessment in complex terrain. In: Proceedings, EWEA
- Sait MA, Chigbu UE, Hamiduddin I, De Vries WT (2019) Renewable energy as an underutilised resource in cities: Germany's 'energiewende' and lessons for post-brexit cities in the united kingdom. Resources. <https://doi.org/10.3390/resources8010007>
- SFOE (2018) Energy strategy 2050 once the new energy act is in force. <https://www.bfe.admin.ch/bfe/en/home/policy/energystrategy-2050.html>. Accessed 26 April 2023
- Federal Administration of Switzerland (2021) Energy. <https://www.eda.admin.ch/aboutswitzerland/en/home/wirtschaft/energie/energie---fakten-und-zahlen.html>. Accessed 8 Feb 2023
- Federal Administration of Switzerland (2022) Hydropower. <https://www.eda.admin.ch/aboutswitzerland/en/home/wirtschaft/energie/die-erneuerbaren-energien.html>. Accessed 5 July 2022
- Wang Y, Hocut CM, Hoch SW, Creegan E, Fernando HJS, Whiteman CD, Felton M, Huynh G (2016) Triple Doppler wind lidar observations during the mountain terrain atmospheric modeling and observations field campaign. *J Appl Remote Sens* 10(2):1–14. <https://doi.org/10.1117/1.JRS.10.026015>
- WSL SLF (2022) WSL SLF institute for snow and avalanche research. <https://www.slf.ch/en/avalanche-bulletin-and-snow-situation/measured-values/description-of-automated-stations.html>. Accessed 2022

Publisher's Note Springer Nature remains neutral with regard to jurisdictional claims in published maps and institutional affiliations.